



Modelling and validation of hot isostatic pressing for additively manufactured FeSi-Inconel composites

Maksim A. Sitnikov¹ · Julien Taurines² · Matti Isakov³ · Suvi Santa-aho³ · Jukka Kuva⁴ · Matthew James Holcomb⁵ · Ira James Holcomb Jr.⁵ · Anouar Belahcen¹

Received: 23 June 2025 / Accepted: 22 October 2025 / Published online: 12 November 2025
© The Author(s) 2025

Abstract

This study explores the development of residual stresses in additively manufactured FeSi–Inconel 625 composites consolidated via hot isostatic pressing (HIP). Residual stress distributions were measured, and a finite element model (FEM) of the HIP process was developed to quantify the contribution of key mechanisms responsible for stress evolution. The model accounts for the mismatch in thermal expansion coefficients, thermal conductivities, and plastic deformation behaviour between the constituent materials. After validation against experimental data, the model was extended to simulate HIP consolidation of the individual materials. The results offer valuable insights into stress development during HIP and provide a framework for optimising the design and manufacturing of multi-material components.

Keywords Residual stress · Modelling · Composites · Additive manufacturing

1 Introduction

The advancement of additive manufacturing (AM) in electromechanical applications has enabled the design and production of complex, high-performance components for electrical machines [1, 2]. These include topologically optimised stators, rotors, and windings that improve efficiency while minimising material usage and enhancing recyclability [3]. One of the significant remaining challenges in AM is the fabrication of multi-material components, particularly the integration of magnetic and non-magnetic materials within a single structure. Successfully addressing this challenge could lead to a paradigm shift in the production of rotors for high-speed synchronous reluctance machines,

enabling significant expansion of their operational speed range.

Previous studies [4] have investigated topologically optimised rotors for synchronous reluctance machines, incorporating magneto-mechanical optimisation to increase torque and reduce mechanical stresses simultaneously. These developments have spurred growing interest in multi-material designs [5], particularly axially laminated anisotropic (ALA) rotors [6]. ALA rotors comprise alternating layers of magnetic and non-magnetic materials, forming a solid structure that provides enhanced mechanical integrity and reduced stress concentrations compared to conventional laminated rotors. However, material selection and processing compatibility remain key challenges despite these advances [7]. Reviews and recent surveys on metal-matrix composites and multi-material AM emphasise the promise of AM for functionally graded and laminated structures, while highlighting persistent issues such as porosity, interfacial bonding, processing-induced anisotropy, and thermal-mismatch-driven stresses [8, 9].

Components produced by laser-based additive manufacturing often require extensive post-processing [10], such as annealing, to relieve residual stresses. Thus, hot isostatic pressing (HIP) directly addresses these issues by healing internal porosity and relieving processing-induced residual stresses, making it an essential post-processing

✉ Maksim A. Sitnikov
maksim.sitnikov@aalto.fi

¹ Department of Electrical Engineering and Automation, Aalto University, Espoo, Finland

² Univ. Grenoble Alpes, CNRS, Grenoble INP, G2Elab, Grenoble 38000, France

³ Faculty of Engineering and Natural Sciences, Tampere University, Tampere, Finland

⁴ Geological Survey of Finland GTK, Espoo, Finland

⁵ Grid Logic Incorporated, Lapeer, MI, USA

step for additively manufactured metallic composites [11]. HIP applies uniform high pressure and temperature to promote pore closure, reduce microstructural anisotropy, and improve key mechanical properties, including tensile strength, ductility, fracture toughness, and fatigue resistance [12]. Experimental work on LPBF Inconel 625 with intentionally induced defects demonstrates HIP's effectiveness in reducing defect size and count, markedly improving fatigue behaviour — for example, increasing the long-crack threshold stress intensity factor from ≈ 7 to $\approx 9 \text{ MPa}\cdot\text{m}^{\frac{1}{2}}$ — although near-surface defects may persist [13]. Industry reports further describe innovations in HIP process parameters and bonding strategies that enhance densification and interfacial strength in complex multi-material builds [14, 15].

Nevertheless, thermal and elastic mismatches between dissimilar materials (e.g., FeSi and Inconel 625) can induce complex residual stress states during the HIP cycle, particularly upon cooling and pressure release [16, 17]. Systematic reviews on AM metal-matrix composite fabrication identify porosity, interfacial reactions, coefficient-of-thermal-expansion mismatch, and microstructural anisotropy as significant uncertainties affecting the mechanical performance of multi-material AM parts, motivating combined experimental and numerical investigations to better understand stress evolution during HIP and optimise process parameters [8, 9].

Despite these advances, a gap remains in systematic studies that integrate detailed experimental residual stress characterisation with finite element modelling of HIP in multi-material AM composites, especially for soft magnetic steels like FeSi combined with high-temperature alloys such as Inconel 625. Existing literature primarily focuses on either porosity reduction or mechanical property improvements, rarely combining both perspectives with modelling of thermal and deformation mismatches.

Moreover, most previous HIP–FEM studies have dealt exclusively with single-material systems [10, 12, 16, 17] and do not address the complex thermo-mechanical interactions that arise in multi-material HIP consolidation. No experimentally validated model currently exists for HIP of dissimilar metallic materials. This study aims to close this gap by developing and validating a coupled thermo-mechanical FEM model for FeSi–Inconel 625 composites, supported by residual stress and porosity measurements.

This study aims to fill this gap by (i) experimentally quantifying residual stresses and porosity before and after HIP in laser powder bed fused FeSi–Inconel 625 composites, and (ii) developing and validating a finite element model of the HIP process incorporating thermal mismatch and deformation mismatch effects. The methodology combines high-energy X-ray diffraction (XRD) for residual

stress measurement, X-ray computed tomography (XCT) for 3D porosity analysis, and FEM simulations reproducing the temperature–pressure–cooling cycle of HIP with realistic material properties and boundary conditions, supported by sensitivity analyses.

The main results include residual stress distribution changes, porosity evolution, and correlation between experimental data and model predictions. These findings are expected to provide quantitative guidance for optimising HIP parameters in multi-material AM components. The outcomes have direct applications in designing high-performance rotors for synchronous reluctance and other electrical machines, where integration of magnetic and non-magnetic materials with controlled residual stresses can significantly enhance operational speed, efficiency, and service life.

2 Manufacturing and modelling

2.1 Manufacturing process

The hot isostatic pressing (HIP) process for metal powder fabrication consists of the following stages:

1. **Deposition of Multi-Metal Powder:** The selected metal powders are deposited into a sealed can, forming the initial preform. This preform is designed to account for an approximately 60% reduction in volume during the densification process.
2. **Deposition of Support Powder:** A layer of support powder is applied around the preform to ensure structural integrity throughout the pressing process.
3. **HIP Processing:** The encapsulated preform is subjected to elevated temperature and pressure within a HIP chamber, following a predefined cycle tailored to the material system. This process promotes densification and reduces internal defects.
4. **Cooling and Machining:** After the HIP cycle, the workpiece is cooled under controlled conditions and subsequently machined to achieve the final dimensions and required surface finish.

Figures 1 and 2 illustrate the HIP setup, the applied thermal and pressure cycle, and the initial geometry of the samples with surrounding support powder.

The materials for HIP fabrication were selected based on their mechanical compatibility and the availability of powder form (Table 1). FeSi is the most widely used soft-magnetic alloy for additive manufacturing in electrical machines [18, 19] due to its favourable magnetic properties. At the same time, Inconel 625 offers excellent strength, corrosion resistance. Thermal expansion coefficients for these two

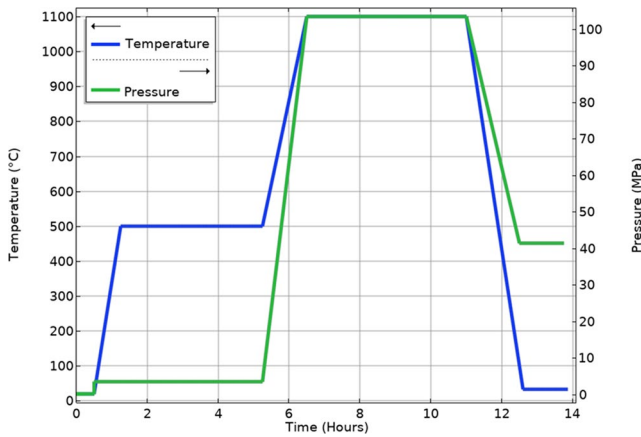


Fig. 1 HIP-cycle

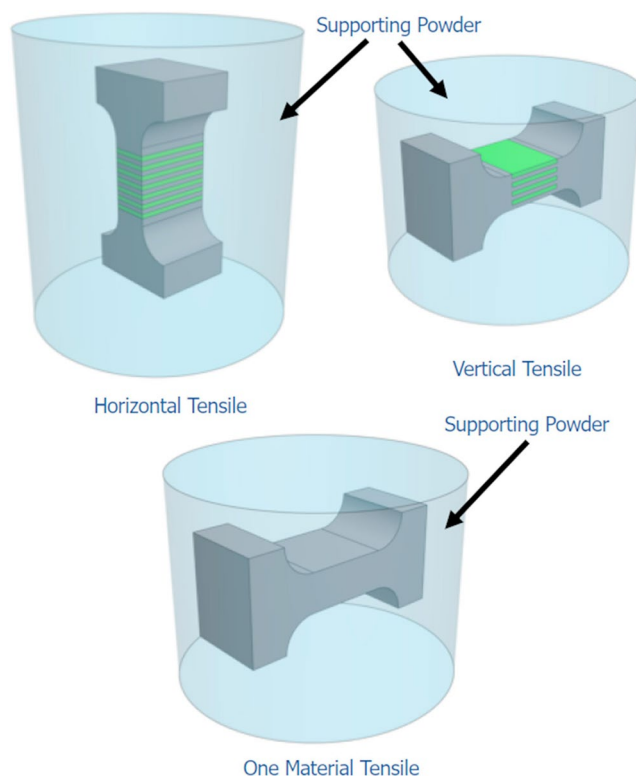


Fig. 2 Multi-metal samples with supporting powder for HIP

Table 1 Expected material properties (at 20 °C)

Parameter	Value	
	FeSi	Inconel 625
Young’s Modulus (GPa)	210	204
Tensile Yield Strength (MPa)	367	414
Tensile Ultimate Strength (MPa)	490	827
Thermal Expansion Coefficient (10 ⁻⁶ /K)	11.27	12.3
Density (kg/m ³)	7350	8400
Saturation Flux Density (T)	1.8	-

materials are sufficiently close ($11.3 \times 10^{-6} \text{ K}^{-1}$ vs. $12.3 \times 10^{-6} \text{ K}^{-1}$) to avoid a significant increase in stress at the interface, ensuring stable bonding during HIP. However, FeSi presents specific challenges: increased Si content leads to brittleness [20], and surface oxidation or Fe₃Si phase formation complicates both processing and stress evaluation.

2.2 XRD and XCT

Residual stresses in the HIP-processed samples were measured using the X-ray diffraction (XRD) technique based on the $\sin^2 \psi$ method [21]. This nondestructive technique relies on the elastic deformation of the crystal lattice, which causes changes in interplanar spacing d and corresponding shifts in diffraction peak positions (Fig. 3) according to Bragg’s law:

$$2d\sin\theta = \lambda \tag{1}$$

where θ is the diffraction angle and λ is the X-ray wavelength; any elastic strain alters d , leading to a shift θ .

To determine the lattice strain ϵ_ψ , the change in interplanar spacing at different tilt angles ψ is measured:

$$\epsilon_\psi = \frac{d_\psi - d_0}{d_0} \tag{2}$$

where d_ψ is measure of the lattice spacing at the tilt angle ψ , and d_0 is the stress-free lattice spacing.

The residual stress is then calculated from the slope of the linear relationship between ϵ_ψ and $\sin^2 \psi$:

$$\begin{cases} \epsilon_\psi = A + B\sin^2\psi \\ \sigma = \frac{E}{1+\nu}B \end{cases} \tag{3}$$

where A represents the strain offset (related to the stress-free lattice spacing), E is Young’s modulus, ν is Poisson’s ratio, $B = \frac{\partial \epsilon_\psi}{\partial (\sin^2 \psi)}$ is the slope of the strain vs. $\sin^2 \psi$ curve.

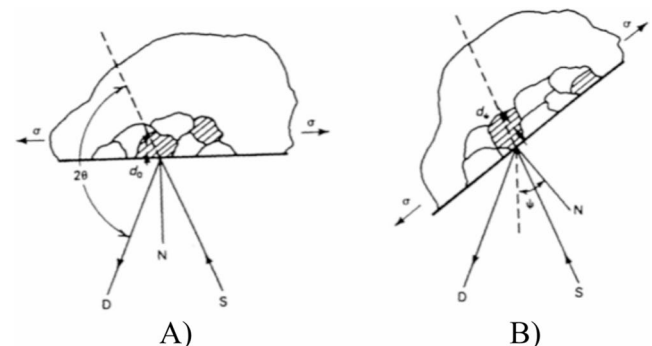


Fig. 3 Principle of XRD stress measurement (A) $\psi = 0$, (B) sample rotated through some known angle $\Psi = \psi_0$ [21]

This method assumes a plane stress condition [21], which is valid for surface-near measurements where the stress normal to the surface is negligible. Consequently, this method determines only the in-plane components of residual stress.

The XRD technique is sensitive to elastic strains within a depth of a few microns [21], making it particularly suitable for assessing surface residual stresses caused by thermal gradients and plastic deformation during the HIP process.

To evaluate the porosity after HIP, X-ray computed tomography (XCT) was performed on representative samples of the FeSi–Inconel composite. XCT enables non-destructive three-dimensional imaging of internal structures with micrometre-scale resolution, making it well-suited for characterising voids and defects resulting from the additive manufacturing process.

The scans were carried out at an accelerating voltage of 180 kV and a tube current of 50 μA , with a power setting of 9 W. A 1.0 mm copper beam filter was applied to reduce beam hardening effects. Images were acquired with a voxel resolution of 9 μm . For each scan, 2700 angular projections were recorded; at each angle, a single 1000 ms exposure was averaged over three exposures to improve signal-to-noise ratio. The total scan time per sample was 180 min. The first two samples were scanned simultaneously with a vertically extended field of view, resulting in a total scan time of 360 min (180 min per sample). Beam hardening correction was applied with a coefficient of 8 (on a dimensionless scale from 0 to 10), and no ring artefact correction was used.

The reconstructed volumetric images were binarised and processed to quantify the porosity. A thresholding technique was applied to separate solid material from voids, followed by morphological filtering to eliminate noise. The total porosity was then computed as the ratio of the void volume to the total volume. This quantitative data was used to estimate the final porosity, validating the predicted porosity evolution during HIP.

2.3 Modelling of the HIP process

The FEM model for the pressing process is based primarily on the multiphysics relationship between two physics: Heat Transfer and Solid Mechanics. It is also worth noting that all physical properties of materials are temperature-dependent.

The equilibrium mechanical equation is written as:

$$\nabla \cdot \sigma = f_v \quad (4)$$

where f_v is the volumetric force vector, σ is the stress related to the strain ϵ through Hooke's law:

$$\sigma = E : (\epsilon - \epsilon^{pl} - \epsilon^{th}) \quad (5)$$

E being the 4th order elasticity tensor. Assuming small strains, one can write

$$\epsilon = \frac{1}{2}(\nabla u + \nabla u^T) \quad (6)$$

Where u is the displacement vector, ϵ^{pl} and ϵ^{th} plastic and thermal strain. In turn, thermal strain is expressed as follows

$$\epsilon^{th} = \alpha (T) (T - T_0) I \quad (7)$$

where I is a second-order unity matrix, α is the material's thermal expansion coefficient, T and T_0 are the working and initial temperatures, respectively.

The Gurson–Tvergaard–Needleman (GTN) porous plasticity model was chosen to describe the shrinkage and densification behaviour of the powder materials during HIP. This model is widely used in modelling porous metal compaction [22] because it can accurately capture the influence of void nucleation, growth, and coalescence on the overall plastic deformation. Compared to the classical Gurson model, the GTN formulation introduces calibration parameters that improve predictive accuracy while maintaining relatively good numerical stability. In contrast to more complex advanced sintering or damage models, GTN provides a balanced compromise between computational efficiency, convergence robustness, and physical realism. Moreover, it requires fewer experimentally derived material parameters, making it suitable for systems with limited complete experimental characterisation, such as powder-based composite materials. The classical von Mises yield function is then modified to the GTN yield function to introduce the volume void fraction f in the mechanical behaviour and is expressed as:

$$Q_{powder} = \left(\frac{3J_2}{\sigma_f} \right) + 2q_1 f_e \cosh \left(\frac{q_2 I_1}{2\sigma_f} \right) - \sigma_f (1 + q_3 f_e^2) \quad (8)$$

where $J_2 = \frac{1}{2}(S : S)$ is the second invariant of the deviatoric stress tensor; $I_1 = tr(\sigma)$ is the first invariant of the Cauchy stress tensor (related to hydrostatic stress); σ_f is the stress of the matrix material; f_e is the effective void volume fraction; q_1 , q_2 and q_3 are model parameters describing the void interaction and coalescence behaviour (usually for metal powders $q_1 = 1.5$, $q_2 = 1$, $q_3 = q_1^2$).

To describe the mechanical behaviour of the zirconium sand, which serves as the support powder during HIP, the Drucker–Prager (DP) plasticity model is used, as it is suitable for granular materials and captures pressure-dependent yielding. The yield function is defined as:

$$Q_{sand} = \sigma_{mises} + a_1 \sigma_m - \sigma_{ys} \quad (9)$$

where σ_{mises} is the von Mises equivalent stress, σ_m is the mean (hydrostatic) stress, a_1 is the pressure sensitivity parameter of the material, σ_{ys} is the yield stress.

The plastic strain rate follows an associated flow rule:

$$\dot{\epsilon}^{pl} = \lambda \frac{\partial Q}{\partial S}, (\lambda \geq 0, Q \leq 0, \lambda Q = 0) \tag{10}$$

where λ is the consistency parameter ensuring the yield condition remains satisfied during plastic loading.

The heat transfer during the HIP process is governed by the transient heat equation, including conduction and advection terms:

$$\rho C_p \frac{\partial T}{\partial t} + \rho C_p u_v \nabla T + \nabla \cdot q = Q_h \tag{11}$$

where ρ material density; C_p specific heat capacity at constant pressure; u_v velocity field (typically negligible in solid materials); $q = -k \nabla T$ is a heat flux and k is the thermal conductivity of the material; Q_h heat source.

The finite element model of the HIP process is shown in Fig. 4, featuring the mesh generated from the original component design (see Fig. 2). To reduce computational complexity and suppress rigid-body motions, three symmetry planes were applied. These symmetry boundary conditions enforce zero normal displacement and zero normal heat flux on the corresponding boundaries.

A mesh sensitivity analysis was conducted to ensure mesh-independent results. Three different mesh densities were tested, and the final mesh was selected based on a compromise between accuracy (less than 2% variation in maximum stress values) and computational cost. The final mesh contains 33,851 elements (Fig. 4).

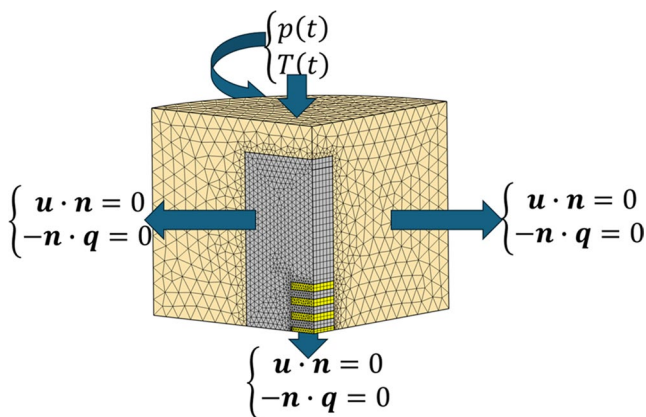


Fig. 4 FEM model of HIP (gray – Inconel625, yellow – FeSi, supporting powder – zirconium sand)

The simulations employed the time-dependent solver with a Fully Coupled approach, using the PARDISO direct linear solver combined with the Automatic Newton nonlinear solver method, which is well suited for transient nonlinear multiphysics problems. Solver tolerances were set to a relative tolerance of 1e-4 and an absolute tolerance of 1e-6. A fixed time step of 0.01 h was chosen to prevent abrupt jumps in plastic deformation, with each time step typically converging within 1 to 3 nonlinear iterations.

Material properties were assigned as temperature-dependent, based on literature data and experimental measurements. The interface conditions between FeSi and Inconel 625 resulted in perfect bonding without slip or delamination.

3 Results and comparison

All simulation results presented in this paper were obtained using COMSOL Multiphysics software. The work was carried out on a PC with the following specifications:

- Processor – 12th Gen Intel(R) Core (TM) i5-12600 K 3.70 GHz.
- Installed RAM – 32 GB.
- System type – 64-bit operating system.
- Windows – Windows 10 Education.

Table 2 shows the comparison of the computational mesh sensitivity analysis.

The results indicate that while the Extra Fine mesh significantly increases computational cost (over 3× longer than Fine), the change in key output parameters (von Mises stress and porosity) compared to Fine is negligible (<0.5%). Therefore, the Fine mesh was selected for all simulations as it provides a good balance between computational efficiency and accuracy, ensuring mesh-independent results.

Table 2 Mesh sensitivity analysis

Parameter	Mesh		
	Normal	Fine	Extra fine
Number of elements, [-]	15,076	33,851	106,667
Computational time, [min]	30	47	174
von Mises' stress in the probe point, [MPa]	319	243	244
Porosity in the probe layer, [%]	4	4.86	4.8

3.1 Shape comparison

Since the main objective of this study is the production and characterisation of composite material, the primary focus of the analysis is placed on the composite specimens. The first comparison was performed for the horizontally oriented composite to assess the accuracy of the predicted workpiece dimensions after HIP. Figure 5 presents the horizontal dog-bone-shaped composite after HIP alongside its numerically modelled counterpart. Table 2 summarises the comparison of key geometric parameters, highlighting the agreement between the experimental and simulated results.

As shown in Fig. 5, the developed model accurately captures the shape distortions induced by the HIP process, including those in regions with sharp geometric transitions. Table 3 demonstrates good agreement between the simulated and experimental results. The observed discrepancies are mainly due to the absence of a metallic container in the model and deviations between the actual properties of the powder material and those reported in the literature. The container was intentionally excluded to avoid introducing complex contact interactions between the metal, the powder, and the supporting zirconium sand, as such interactions significantly increase computational cost and often lead to convergence issues. For this reason, the focus was placed on modelling the workpiece and its supporting medium, which still yielded sufficiently accurate predictions for validation. It should also be noted that the omission of explicit contact conditions with the zirconium sand and container does not significantly affect the predicted local strain and stress fields, as the HIP process applies uniform hydrostatic pressure. The supporting sand deforms together with the workpiece, acting as a compliant medium with much lower stiffness than the metallic composite.

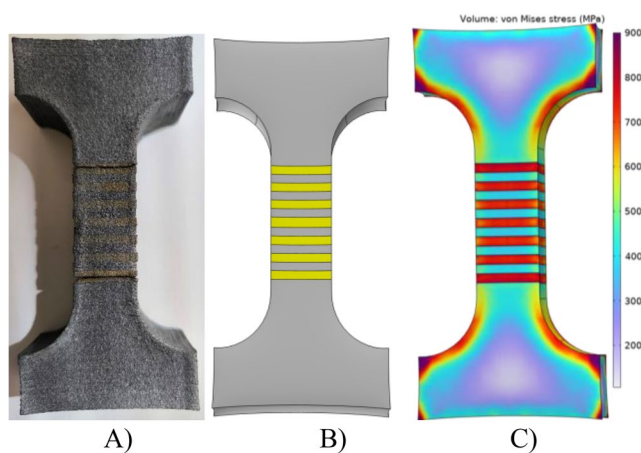


Fig. 5 Comparison of the horizontal composite sample shape from HIP (A) and from the FEM model (B), stress distribution in original horizontal composite (C)

Table 3 Geometric parameters comparison

Parameter	Value		
	Experiment	Model	Difference
Length, [mm]	121.6	137	15.4 (12.6%)
Width of layered part, [mm]	18.2	22	3.6 (19.7%)
Depth, [mm]	20	23.5	3.5 (17.5%)

Furthermore, Fig. 5 (C) shows the von Mises stress distribution obtained from the FEM model, revealing stress concentrations precisely in the same regions where fracture occurred in the experimental sample. This correlation confirms that the model correctly predicts the zones of maximum thermo-mechanical loading without explicitly defining delamination or contact failure. The observed fracture in the FeSi layer (Fig. 5A) can therefore be attributed to the mismatch in the coefficients of thermal expansion between the constituent materials and the constrained deformation caused by the surrounding zirconium sand.

To mitigate this issue, the configuration was revised so that the FeSi layers were fully enclosed by Inconel 625, as shown in Fig. 4. Figure 6 presents a comparison between the final shape of the modified sample with Inconel support after HIP and the corresponding FEM simulation results. As demonstrated in Fig. 6, the model reliably predicts the final geometry of the sample, even when additional supporting material is introduced.

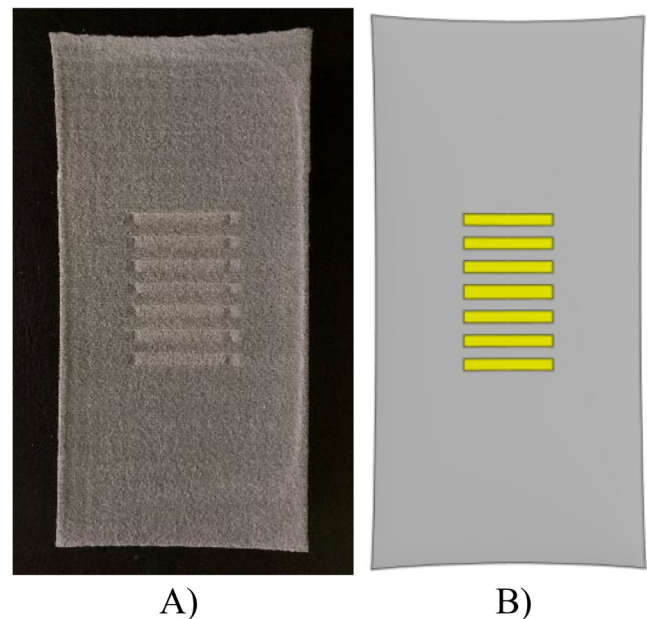


Fig. 6 Comparison of the modified horizontal composite sample shape from HIP (A) and from the FEM model (B)

3.2 Residual stresses

Measurements were taken at various points, as shown in Fig. 7, within the composite.

As an example, this section highlights two representative data points from the complete set of measurements presented in Table 4.

For statistical evaluation of the obtained results, standard metrics were used: Mean Absolute Error (MAE), Root Mean Square Error (RMSE), and the coefficient of determination (R^2), which are calculated as follows:

$$\left\{ \begin{array}{l} MAE = \frac{1}{N} \sum_{i=1}^N |M_i - E_i| \\ RMSE = \sqrt{\frac{1}{N} \sum_{i=1}^N |M_i - E_i|^2} \\ R^2 = 1 - \frac{\sum_{i=1}^N |M_i - E_i|^2}{\sum_{i=1}^N |E_i - \bar{E}|^2} \end{array} \right.$$

where M_i is the model value, E_i is the measured value, \bar{E} is the average of the measured values, N is the number of points.

The comparison for Inconel 625 shows good agreement between the experimental measurements and the developed model results. Notably, point B3 was located in a region that had undergone post-processing, including milling and electrical discharge machining (EDM), to extract

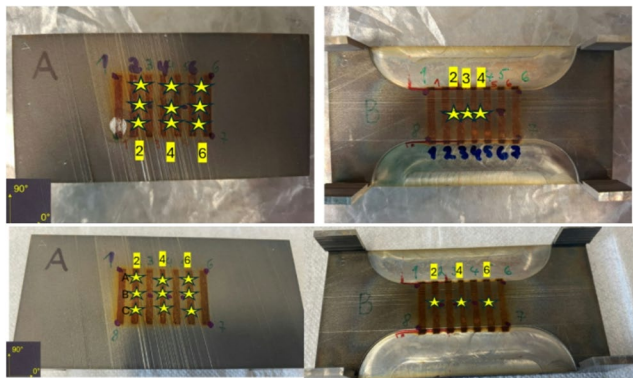


Fig. 7 Measurement points in Inconel 625 (top) and FeSi (bottom) in the horizontal cross-section of the composite. The points are labelled using the format Xn–Y, where X indicates the side (A or B), n is the column number, and Y is the row number

Table 5 Statistical quantification of the stresses

Material	MAE (MPa)	RMSE (MPa)	R^2
Inconel 625	36.2	40.9	0.73
FeSi	61.7	66.6	–1.53

dog-bone-shaped specimens. Table 5 shows that neither of these machining operations introduced significant deviations from the predicted geometry, indicating that the model remains accurate even after local processing.

To quantitatively evaluate the agreement, key error metrics were calculated. The mean absolute error (MAE) between model predictions and measured stresses across six measurement points is approximately 36 MPa, and the root mean square error (RMSE) is around 41 MPa. The coefficient of determination (R^2) is 0.73, indicating a strong correlation between the model and measurements. Considering the experimental uncertainty ranges, which vary approximately between ± 28 MPa and ± 53 MPa depending on the measurement location, the model predictions fall mostly within or close to the experimental confidence intervals. These quantitative error margins confirm that the model adequately captures the stress state in Inconel 625 under the tested conditions.

In contrast, the measurements for FeSi exhibit greater uncertainty. This discrepancy is attributed to the presence of a surface oxide layer and the formation of secondary phases during processing. Although various cleaning methods were tested, including citric acid treatment and electrolytic etching, none proved sufficiently effective or consistent to justify their application to all measurement locations. Representative examples of the measurement data for FeSi and Inconel 625 are shown in Figs. 8 and 9, respectively, illustrating the differences in measurement consistency and reliability between the two materials.

Similar error metrics were calculated for FeSi. The mean absolute error (MAE) was approximately 62 MPa, and the root mean square error (RMSE) was about 67 MPa, which are notably higher than for Inconel 625. The coefficient of determination (R^2) was negative (–1.53), indicating poor correlation between model and experimental data for FeSi. This suggests that the current model requires further refinement

Table 4 Residual stresses comparison

Stress component	Measurement location					
	A2_A		A4_B		B3	
Inconel 625	Measured	Model	Measured	Model	Measured	Model
σ_{90} (MPa)	332±33	292	299±38	319	297±47	318
σ_{00} (MPa)	116±28	150	157±33	131	205±53	129
FeSi	Measured	Model	Measured	Model	Measured	Model
σ_{90} (MPa)	122±47	50	75±80	33	–8±65	–65
σ_{00} (MPa)	63±71	146	86±92	182	109±72	129

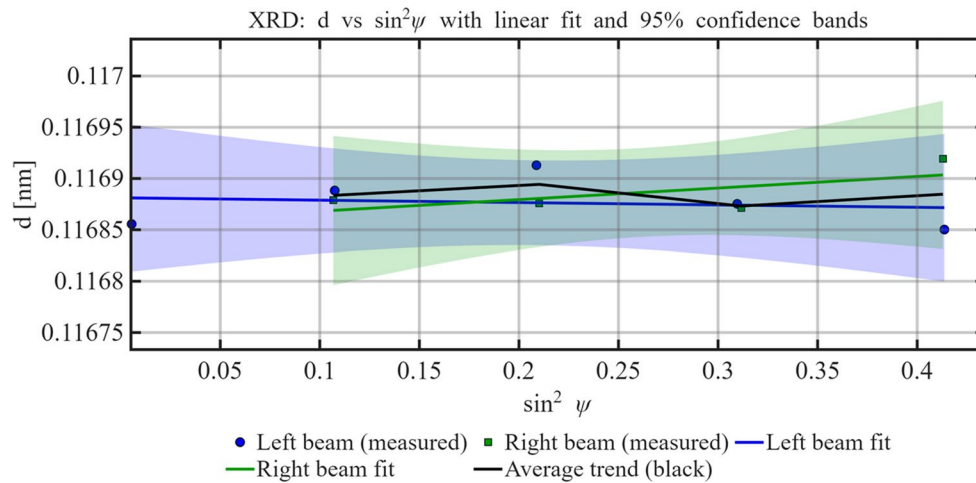


Fig. 8 X-ray diffraction results for FeSi obtained using a Stresstech XStress 3000 diffractometer with $\text{CrK}\alpha$ radiation and two symmetrically placed X-ray detectors. The plot shows interplanar spacing d vs. $\sin^2\psi$; blue circles and green squares correspond to measurements

from the two separate X-ray beams, and the respective linear regressions are shown in red and blue. The black line denotes the average trend. The average full width at half maximum (FWHM) of the fitted diffraction peaks was approximately 4.3° (ranging from 3.57° to 4.45°)

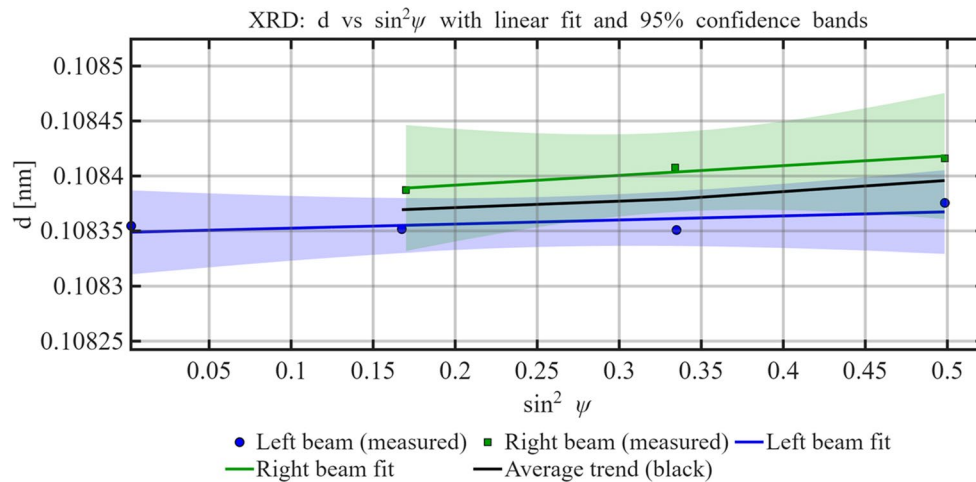


Fig. 9 X-ray diffraction results for Inconel 625. The measurement procedure and legend follow those described in Fig. 8. The average FWHM of the FeSi diffraction peaks was approximately 2.1° (ranging from 2.0° to 2.3°)

to accurately capture the stress state in FeSi under the tested conditions. Future refinements will focus on a more detailed investigation of the metallurgical phases present in FeSi and their integration into the constitutive description, which is expected to improve the predictive accuracy of the model.

The FeSi sample exhibited broad data scattering and limited linearity in the d vs. $\sin^2\psi$ plot, resulting in a poorly defined residual stress estimate. Moreover, the diffraction peaks were asymmetric with noticeable shoulders, suggesting the presence of a secondary phase, most likely Fe₃Si. In contrast, the Inconel sample demonstrated a consistent and linear response, yielding a more reliable residual stress value. The broader FWHM of Inconel peaks (4.16° on average, compared to 2.15° for FeSi) suggests either a finer grain

structure or a higher density of crystal defects, such as dislocations. This interpretation is consistent with established diffraction theory [23], although further investigation (e.g., transmission electron microscopy, TEM, or electron backscatter diffraction, EBSD) would be required to distinguish the dominant mechanism. However, the single-phase nature of Inconel and the absence of peak asymmetry suggest a more homogeneous response to HIP processing. These results confirm that Inconel retains a stable and uniform microstructure post-HIP. In contrast, FeSi is more prone to phase separation and heterogeneity, which adversely affects its mechanical and magnetic properties.

Thus, only the Inconel 625 measurements can be considered reliable regarding model verification, as they

demonstrate good agreement with the simulation results. In contrast, the assessment of residual stresses in the FeSi component remains inconclusive due to the presence of secondary phases and a persistent oxide layer. Further analysis is required to accurately characterise these effects and enable meaningful validation of the model for FeSi.

3.3 Porosity

For porosity quantification, cross-sectional optical images of local sample areas were analysed. In total, three images were acquired for each material, taken at different depths within the sample to account for possible through-thickness variations in porosity. The scanned regions were 2×2 mm in size, providing a representative sampling area while maintaining sufficient resolution (9 microns) for defect detection. The images were processed using grayscale threshold binarisation, where a fixed threshold value was applied to distinguish pores from the matrix material. This approach allowed for consistent pore area fraction calculation across all samples.

Figure 10 presents the original tomography image used to evaluate the porosity of the composite sample. Figure 10.B illustrates the image processing workflow, which includes region selection, grayscale conversion, and subsequent binarisation.

Following binarisation, the total number of pixels is compared to those exceeding a predefined threshold value. The ratio of these pixel counts is used to estimate the material's porosity.

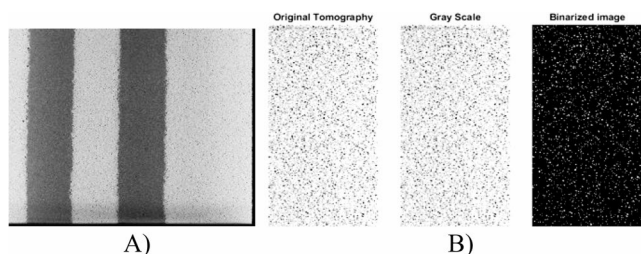


Fig. 10 Original sample's tomography (A) and binarisation of a tomography scan (B)

Fig. 11 Porosity (in %) from the Multiphysics FEM model

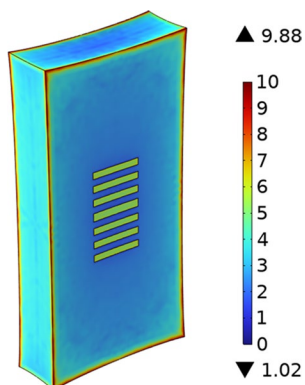


Table 6 Geometric parameters comparison

Image	Porosity, %
1	5.1
2	4.9
3	5.17

Figure 11 shows the distribution of porosity in the FEM model.

The comparison was made for a single Inconel layer by averaging the porosity value over the domain. In this case, the composite porosity was approximately 5%, which is quite consistent with the modelling result of 4.8%.

Table 6 shows a comparison of porosity in Inconel layers for three scanned images. Results for the model are not shown because the samples were taken randomly from an unknown cutting depth.

Based on the data in Table 6, the samples can be considered homogeneous in terms of porosity, which corresponds to the model in Fig. 11. To ensure statistical relevance, porosity was evaluated in three different regions taken at varying depths of the consolidated sample. The close agreement among all measurements (4.9–5.2%) confirms that the results are representative of the overall material volume and therefore suitable for model validation.

4 Discussion

The developed finite element model of the HIP process demonstrated good predictive capability in estimating the final geometry and residual stress evolution in Inconel 625 and FeSi–Inconel 625 composites. For Inconel 625, the comparison between the simulated and experimental geometries showed close agreement, even in samples subjected to post-processing such as milling and EDM. This indicates that the model reliably captures the key thermomechanical phenomena occurring during HIP consolidation.

However, results for the FeSi region showed higher uncertainty. XRD analysis revealed the presence of secondary phases, potentially including Fe_3Si , as well as a persistent oxide layer, which influenced the residual stress measurements. These effects introduce challenges in the reliable assessment of stress states in FeSi, representing a significant methodological limitation of the current study. The oxidation and phase transformations complicate the interpretation of diffraction data, especially when stress evaluation is based on specific crystallographic planes (e.g., (211)), which may be affected by phase heterogeneity and surface contamination. The limitations of XRD-based residual stress measurements in multi-phase materials such as FeSi become particularly pronounced in the presence of oxide layers and

secondary phases. The overlapping diffraction peaks from different phases can bias stress evaluation, while surface oxides introduce additional strain fields that may not represent the bulk material. Moreover, XRD probes only a shallow surface layer, making it sensitive to surface conditions rather than the actual internal stress state. These factors reduce the accuracy and reliability of residual stress determination in complex multi-phase systems using XRD alone.

Nevertheless, despite the limitations of XRD analysis, the FEM model can be regarded as partially validated. The good agreement was obtained for Inconel 625 residual stress ($R^2 = 0.73$) and the consistent porosity prediction (4.8% simulated vs. $\approx 5\%$ measured).

In the present FEM model, the mechanical and thermal properties of FeSi were not adjusted to account for the formation of surface oxides or secondary Fe₃Si phases, as the oxide layer is relatively thin compared to the sample. It was therefore considered that the mechanical and thermal properties of FeSi were those of an ideal material in the present FEM model. Further microstructural analysis is required to quantify their influence on the effective behaviour of the material before such effects can be incorporated into the constitutive model.

The primary source of deviation between FEM-predicted and experimentally measured geometries is the limited availability of physical property data for FeSi over a broad temperature range, which is essential for accurately modelling the HIP process. Additionally, the 3D plastic deformation model includes certain simplifications: contact interactions between dissimilar materials and between the powder bed (sand) and the container were not modelled. These interactions can influence local strain and geometry but were omitted to improve numerical stability and computational efficiency, as contact conditions in plasticity problems can be highly resource-intensive and prone to instability.

The main trade-offs between computational cost and simulation accuracy arise from the need to simplify the computational grid. The physical complexity of HIP, characterised by large plastic deformations, does not allow for simplification at the material behaviour level through analytical or semi-analytical approaches. In this work, mesh resolution was adjusted to balance accuracy and computational time, as summarised in Table 2, which compares simulation runtime and relative error. This illustrates the trade-off in computational resource demands. For geometries such as purely cylindrical samples with concentric layers, further simplification could be achieved by replacing the complete 3D model with a 2D axisymmetric formulation, reducing computational cost without significantly compromising accuracy.

When considering the limitations in XRD-based residual stress measurements, several factors should be considered. Surface oxidation during HIP introduces additional diffraction peaks, complicating peak fitting and shifting measured lattice spacings. Secondary phase formation, such as Fe₃Si, changes the diffraction pattern, making phase-specific stress analysis challenging. Moreover, the shallow penetration depth of X-rays causes the measurement to reflect primarily near-surface conditions, which may differ from bulk stresses. Consequently, XRD results for FeSi should be interpreted cautiously, and complementary techniques such as neutron diffraction or synchrotron XRD are recommended for future studies.

The porosity estimation from X-ray tomography confirmed the model's prediction with reasonable accuracy, showing only a slight deviation (5% measured vs. 4.8% simulated), further supporting the model's validity. The GTN plasticity model proved.

Despite the overall good agreement between simulations and experiments, the remaining discrepancies observed for FeSi highlight the need for a more detailed temperature-dependent calibration of its mechanical and thermal properties. Future work should focus on experimentally determining these parameters under HIP-relevant conditions to further improve the predictive accuracy of the FEM model.

Although the tensile testing was not part of the FEM validation, it provides an essential complementary confirmation of the mechanical feasibility of the proposed multi-material concept. The representative result shown in Fig. 12 demonstrates that the horizontally oriented FeSi–Inconel composite exhibits a tensile strength exceeding 120 MPa, which is a satisfactory value for this class of HIP-consolidated structures intended for high-speed applications [24]. This experimental observation supports the practical applicability and structural reliability of the fabricated composites, despite the simplifications introduced in the current modelling framework.

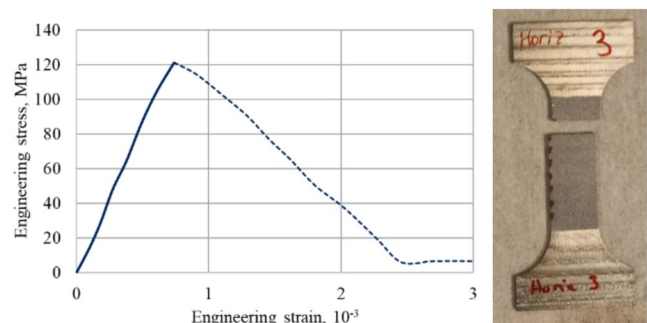


Fig. 12 Representative example tensile test result for the horizontally oriented FeSi–Inconel 625 composite (A) and one of the specimens after test (B)

5 Conclusion

This study presented an integrated experimental and numerical investigation of residual stress formation in FeSi–Inconel 625 composites produced via hot isostatic pressing (HIP). A finite element model based on porous plasticity was developed and compared with geometry measurements, porosity analysis, and residual stress data.

The model showed good agreement for Inconel 625, providing consistent predictions of shape distortions and porosity. For FeSi, the presence of secondary phases and surface oxidation introduced significant uncertainty in the XRD-based residual stress assessment, underlining the limitations of diffraction techniques when applied to multi-phase materials. These findings indicate the need for further characterisation and refinement of the constitutive description for FeSi. The GTN plasticity model proved adequate for simulating powder densification, offering a reasonable balance between computational efficiency and physical fidelity.

Although the current validation for FeSi residual stresses remains limited, the results demonstrate that HIP can be effectively used to consolidate dissimilar metallic powders into mechanically sound multi-material structures. The developed framework provides a useful basis for analysing stress evolution and deformation behaviour in such composites.

Future work will focus on extending the model with temperature-dependent material properties and on integrating tensile testing to assess the mechanical performance of FeSi–Inconel composites under representative loading conditions. Additional studies will address post-HIP treatments aimed at reducing residual stresses and improving microstructural uniformity, as well as optimising the initial geometry of composite parts to minimise distortion and improve dimensional accuracy.

Funding Open Access funding provided by Aalto University. This work was supported by the Academy of Finland Centre of Excellence in High-Speed Electromechanical Energy Conversion Systems (Grant number 346438).

Data Availability The data that support the findings of this study are available from the corresponding author upon reasonable request.

Declarations

Conflict of interest The authors have no relevant financial or non-financial interests to disclose.

Generative AI and AI-assisted technologies in the writing process During the preparation of this work the authors used ChatGPT (OpenAI) to improve the clarity, grammar, and style of the manuscript text. After using this tool, authors carefully reviewed and edited the content to ensure accuracy and take full responsibility for all scientific content and conclusions presented in the article.

Open Access This article is licensed under a Creative Commons Attribution 4.0 International License, which permits use, sharing, adaptation, distribution and reproduction in any medium or format, as long as you give appropriate credit to the original author(s) and the source, provide a link to the Creative Commons licence, and indicate if changes were made. The images or other third party material in this article are included in the article's Creative Commons licence, unless indicated otherwise in a credit line to the material. If material is not included in the article's Creative Commons licence and your intended use is not permitted by statutory regulation or exceeds the permitted use, you will need to obtain permission directly from the copyright holder. To view a copy of this licence, visit <http://creativecommons.org/licenses/by/4.0/>.

References

1. Tiismus H, Kallaste A, Belahcen A, Rassõlkin A, Vaimann T (2019) Challenges of additive manufacturing of electrical machines. 2019 IEEE 12th international symposium on diagnostics for electrical machines, power electronics and drives (SDEMPED), Toulouse, France, pp. 44–48. <https://doi.org/10.1109/DEMPED.2019.8864850>
2. Vaimann T, Tiismus H, Kallaste A (2023) Concepts of additively manufactured electrical machines and components. 2023 23rd international scientific conference on electric power engineering (EPE), Brno, Czech Republic, pp. 1–6. <https://doi.org/10.1109/EPE58302.2023.10149252>
3. Ahmed Selema M, Beretta M, Van Coppenolle H, Tiismus A, Kallaste MN, Ibrahim M, Rombouts J, Vleugels, Leo AI, Kestens PS (2023) Evaluation of 3D-printed magnetic materials for additively-manufactured electrical machines. *J Magn Mater*, 569:170426, <https://doi.org/10.1016/j.jmmm.2023.170426>
4. Belahcen A, Sitnikov MA, Galunin SA (2021) Optimisation of a high-speed synchronous reluctance machine's rotor topology. 2021 international conference on electrotechnical complexes and systems (ICOECS), Ufa, Russian Federation, pp. 279–284. <https://doi.org/10.1109/ICOECS52783.2021.9657390>
5. Nazir A et al (2023) Multi-material additive manufacturing: a systematic review of design, properties, applications, challenges, and 3D printing of materials and cellular metamaterials. *Mater Design* vol. 226. Elsevier BV, p. 111661. <https://doi.org/10.1016/j.matdes.2023.111661>
6. Abramenko V, Petrov I, Nerg J, Pyrhönen J (2020) Synchronous reluctance motors with an axially laminated anisotropic rotor as an alternative in high-speed applications. *IEEE Access* 8:29149–29158. <https://doi.org/10.1109/ACCESS.2020.2971685>
7. Scherman E et al (2023) Different rotors of an axially-laminated-rotor synchronous reluctance machine – assessment of effects of materials and manufacturing methods. 2023 IEEE international electric machines & drives conference (IEMDC), San Francisco, CA, USA, pp. 1–7. <https://doi.org/10.1109/IEMDC55163.2023.10238976>
8. Pallab Sarmah K, Gupta (2024) Recent advancements in fabrication of metal matrix composites. *Syst Rev Mater* 17(18):4635. <https://doi.org/10.3390/ma17184635>
9. Mohan Sai Kiran Kumar Yadav Nartu, Agrawal P (2025) Additive manufacturing of metal matrix composites. *Mater Design* 252:113609. <https://doi.org/10.1016/j.matdes.2025.113609>
10. Puskar Pathak, Mohan Sai Kiran Kumar Yadav Nartu (2025) Additive manufacturing of soft magnetic high entropy alloys: a review. *J Magn Mater* 627:173148. <https://doi.org/10.1016/j.jmmm.2025.173148>

11. Additive manufacturing using multi-material 3D powder printing technology grid logic, [Accessed: June 9, 2025]. Available: <https://www.grid-logic.com/>
12. Zhou S, Song B, Xue P et al (2017) Numerical simulation and experimental investigation on densification, shape deformation, and stress distribution of Ti6Al4V compacts during hot isostatic pressing. *Int J Adv Manuf Technol* 88:19–31. <https://doi.org/10.1007/s00170-016-8687-0>
13. Jean-René Poulin A, Kreitzberg V, Brailovski (2021), article Effect of hot isostatic pressing of laser powder bed fused inconel 625 with purposely induced defects on the residual porosity and fatigue crack propagation behavior. *Additive Manuf* 47:102324. <https://doi.org/10.1016/j.addma.2021.102324>
14. Hot isostatic pressing: improving quality and performance in AM parts production," *Metal-AM* (Metal Additive Manufacturing magazine), (article/report), (Metal-AM archive). Accessed Aug 10, 2025
15. Combining metal AM and hot isostatic pressing (HIP): application and process innovations. *Metal-AM* (Euro PM/technical session summary), (2017 report/coverage). Accessed Aug 10, 2025
16. Haoyi Niu Z, Liu H, Wang H, Wu Q, Liu, Guohua F (2025) Effects of hot isostatic pressing on the micron-scale residual stress of nickel-based single-crystal superalloys. *J Mater Sci Technol* 221:102–116. <https://doi.org/10.1016/j.jmst.2024.09.036>
17. Qin S, Herzog S, Kaletsch A, Broeckmann C (2021) Effects of pressure on microstructure and residual stresses during hot isostatic pressing post treatment of AISI M50 produced by laser powder-bed fusion. *Metals* 11:596. <https://doi.org/10.3390/met11040596>
18. Newman D et al (2025) Development of solid synchronous reluctance rotors with multi-material additive Manufacturing. In *IEEE transactions on industry applications*. March-April 61(2):2911–2923. <https://doi.org/10.1109/TIA.2024.3522210>
19. Di Nardo M et al (2025) Experimental assessment of a synchronous reluctance machine featuring an additive manufactured rotor. 2025 IEEE workshop on electrical machines design, control and diagnosis (WEMDCD), Valletta, Malta, pp. 1–6. <https://doi.org/10.1109/WEMDCD61816.2025.11014166>
20. Gaoyuan O, Chen X, Liang Y, Macziewski C, Cui J (2019) Review of Fe-6.5 wt%Si high silicon steel—a promising soft magnetic material for sub-kHz application. *J Magn Magn Mater* 481:234–250. <https://doi.org/10.1016/j.jmmm.2019.02.089>
21. Prevéy PS (1986) X-ray diffraction residual stress techniques. *Metals handbook*. 10. Metals Park: American Society for Metals, 380–392
22. Haowei Guo H, Wang X, Li Z, Dong L, Zhang W, Li (2024) Investigation of mechanical properties of laser powder bed fused AlSi10Mg lattice structures using GTN damage model. *J Mater Res Technol*, 29: 1937–1948. <https://doi.org/10.1016/j.jmrt.2024.01.187>
23. Warren BE (1990) X-ray diffraction. Dover Publications, Mineola, New York
24. Sitnikov MA, Taurines J, Belahcen A (2025) Effect of axial slits on high-speed axially laminated rotor of synchronous reluctance machine. 2025 IEEE workshop on electrical machines design, control and diagnosis (WEMDCD), Valletta, Malta, pp. 1–6. <https://doi.org/10.1109/WEMDCD61816.2025.11014112>

Publisher's note Springer Nature remains neutral with regard to jurisdictional claims in published maps and institutional affiliations.